ACS APPLIED NANO MATERIALS

www.acsanm.org Article

# Tailoring Gold Nanoisland-Based Biosensors for Ultrasensitive Detection of Doxorubicin in Biological Fluids

Alessandra Quarta, Simona Bettini,* Massimo Cuscunà, Daniela Lorenzo, Gianmichele Epifani, Giuseppe Gigli, Ludovico Valli, Jamil A. Aliyev, Elkhan E. Kazimov, Matanat J. Bakhishova, Oktay K. Gasymov, and Daniela Simeone*

Cite This: *ACS Appl. Nano Mater.* 2024, 7, 18724−18736 Read Online

ACCESS | Metrics & More | Article Recommendations | Supporting Information



**ABSTRACT:** Recent advancements in medical science have ushered in the era of "Personalized Medicine," which tailors treatments to individual genetics, lifestyle, and environmental factors. A cornerstone of this approach is continuous monitoring and adjustment of treatment regimens to optimize effectiveness while minimizing side effects. In therapeutic drug monitoring (TDM), crucial for drugs like doxorubicin (DOX) with severe side effects, traditional methods such as spectrofluorimetry and chromatography are utilized, but they suffer from cost and complexity issues. Biosensors, especially those leveraging Localized Surface Plasmon Resonance (LSPR) and surface-enhanced Raman spectroscopy (SERS), offer a promising alternative. This study focuses on developing a cost-effective plasmonic biosensor using gold nanoislands semiembedded in a glass substrate. The LSPR platform, based on gold nanoislands (Au NIs) with an average diameter of 23 nm, offers a rapid method for ultrasensitive, label-free detection of DOX in biological fluids up to the nanomolar range, even in diluted (1:10) and undiluted blood serum samples from cancer patients receiving the drug. The method capitalizes on the extraordinary adhesion between the nanoislands and the glass matrix, preserving plasmon integrity while enhancing the electric field surrounding the nanoislands for improved sensitivity. Moreover, by exploiting nanoislands with $Au/Al_2O_3$ core/shell structures with an average diameter and gap of about 70 and 7 nm, respectively, highly efficient SERS-active platforms are created, enabling the detection of ultralow DOX concentrations down to picomolar range, where the LSPR system is insensitive. The combined use of both systems enables the detection of DOX across a broad range, from low to high nanomolar concentrations, in biological fluids. This integration of semiembedded nanoislands presents a scalable and multifunctional approach suitable for point-of-care diagnostics, offering reproducible and stable characteristics over time.

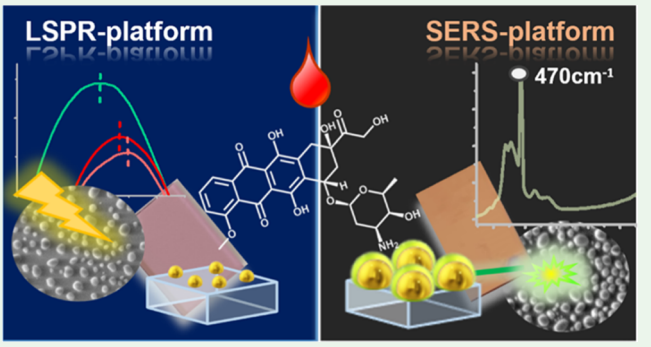


**KEYWORDS:** *therapeutic drug monitoring, biosensor, gold nanoisland, LSPR shift, SERS*

## 1. INTRODUCTION

Recent advancements in medicine and technology have given rise to the era of "Personalized Medicine," a paradigm that tailors therapies to individual lifestyle, genetic variations, and environmental factors. This approach involves identifying unique physiological parameters for each patient to customize effective treatment regimens. Personalized medicine also emphasizes continuous monitoring of patient care cycles and health data, allowing for dynamic adjustments to meet individual needs, such as personalized drug dosages and durations to optimize therapeutic efficacy while minimizing adverse side effects.[1,2]

In the realm of therapeutic drug monitoring (TDM), a critical task for drugs with substantial toxicity profiles, doxorubicin (DOX) stands out due to its severe side effects. DOX, an anthracycline antineoplastic agent widely used to treat various solid tumors,[3−5] disrupts cellular DNA, halting cell proliferation.[6,7]

Traditional quantification of DOX levels in biological fluids relies on analytical techniques like spectrofluorimetric measurements and chromatographic methods, including High Performance Liquid Chromatography (HPLC) coupled with mass spectrometry.[8−10] While HPLC and mass spectrometry offer enhanced sensitivity compared to spectrofluorimetric procedures, they are also more time-consuming and expensive

**Received:** March 27, 2024
**Revised:** July 24, 2024
**Accepted:** July 25, 2024
**Published:** August 3, 2024




https://doi.org/10.1021/acsanm.4c01827
*ACS Appl. Nano Mater.* 2024, 7, 18724−18736

and require specialized personnel and laboratories. Consequently, the results cannot be obtained in real time at the patient's bedside.

In contrast, biosensors offer a promising alternative, characterized by their cost-effectiveness, versatility, and rapid response times. This class of devices includes various types of biosensor, such as electrochemical and optical sensors.[11−15] Optical biosensors based on the surface plasmon resonance (SPR) effect are particularly noteworthy due to high sensitivity, simplicity of design and large-scale production.[16] In particular, localized surface plasmon resonance (LSPR)-based devices represent the last frontier for label-free biosensors capable of exploiting the phenomenon of plasmon resonance to measure low concentrations of analytes, drug discovery, and screening. Noble metal nanoparticles (NPs) were extensively used in LSPR-sensors for their sensitivity to variations in the refractive index (RI) upon molecular interactions at the metal surface, leading to a shift of the resonance peak wavelength.[17−21] The effects of the particles' size, shape, spatial organization, and surface coating on the analytical performance of the resulting sensors have also been investigated.[22−24]

Surface-Enhanced Raman Spectroscopy (SERS) stands out as an alternative and highly sensitive technique for TDM.[25] This method provides fingerprint-type molecular recognition characteristic of vibrational spectroscopic techniques and offers high Raman signal amplification, resulting in a sensitivity $10^4$−$10^8$ times greater than classical Raman spectroscopy. SERS enables the detection of single molecules, and various substrates have been proposed with detection limits in the nanomolar (nM) range.[26−30]

The widespread use of Au nanostructures across numerous research areas[31] has driven the development of two primary fabrication techniques based on top-down and bottom-up approaches. While electron-beam lithography (EBL) and nanoimprint lithography (NIL) offer high-precision control, they are constrained by high costs, small-area processing capabilities, limited processing areas, and the need for sophisticated and expensive equipment. Conversely, self-assembly, dip coating, and electrochemical deposition are scalable techniques suitable for large-area fabrication, although these methods can be time-consuming and labor-intensive.

In this study, a low-cost, lithographic-free, and readily manufacturable plasmonic biosensor was developed utilizing gold nanoislands, semiembedded into commercial inexpensive glass substrates for ultrasensitive label-free detection of DOX in various biological fluids.

The use of glass makes the dewetting process advantageous over other emerging plasma technologies, i.e., microplasma (MP), for the fabrication of plasmonic nanostructures which typically require a conductive layer such as indium tin oxide (ITO). The inclusion of ITO can alter the plasmon characteristics, thereby diminishing the performance. Additionally, MP necessitates a porous substrate for efficient mass transport, particularly for large surface areas.[32,33] The distinctive feature of our platform lies in the extraordinary adhesion between the nanoislands and the glass matrix that preserves the plasmon integrity while concurrently amplifying the electric field surrounding the NIs. This enhancement significantly improves the efficiency of DOX detection, achieving nanomolar sensitivity, as with classical LSPR spectroscopy.

Tailoring Au nanoislands into Au/$Al_2O_3$ core/shell nanostructures, through dielectric coating, allows the generation of highly efficient SERS-active structures

Owing to its well-established biocompatibility,[34] $Al_2O_3$ is an excellent candidate for precisely regulating electron and energy transfer between adjacent Au nanoislands (Au NIs) and DOX molecules. Additionally, $Al_2O_3$ facilitates a more pronounced LSPR shift and intensifies local electromagnetic (EM) field strengths compared to $SiO_2$, both of which were tested for this platform. This tailored design enables the sensitive detection of ultralow DOX concentrations in the picomolar range.

Therefore, the integration of semiembedded nanoislands, based on Solid State Dewetting (SSD), represents a strategy for creating a large-area, multifunctional platform suitable for point-of-care and real-time health diagnostics, with highly reproducible and stable characteristics over time. Furthermore, appropriate functionalization of the platform with an organic linker opens up possibilities for innovative nanoplasmonic bioapplications, including virus detection, tumor detection, biological imaging, and drug detection.[35,36]

## 2. EXPERIMENTAL METHOD

**2.1. Materials.** Gold (99.99% purity) was purchased from Umicore (Belgium), doxorubicin and fetal bovine serum (FBS) were purchased from Sigma-Aldrich, and ultrapure water (resistivity 18.2 MΩ·cm) was used for solution preparation and sensor surface washing. Human serum (HS) samples were provided by the National Center of Oncology of the Republic of Azerbaijan (Baku, Azerbaijan).

**2.2. Fabrication Process of Au NIs and Au/$Al_2O_3$ NIs.** Gold nanoislands were fabricated through thermal evaporation of gold onto microscope glass slides (25.4 mm × 76.2 mm, 1.0 mm thick) followed by thermal dewetting. In each step, a 5 nm thick gold layer was evaporated onto the slide without the need of any adhesion layer and then annealed in air at 585 °C. The heating ramp rate was set to 20 °C $min^{-1}$, followed by 3 h of soaking time at the maximum temperature. This cycle (Au deposition/thermal dewetting) was repeated three times. The first dewetting defines the mean spatial period of the NI disordered array, while the next two cycles promote the lateral growth of the formed NIs. Then, a thin aluminum oxide shell was deposited by using a plasma-enhanced atomic layer deposition (PE-ALD) from Senthec Instruments. In detail, the ALD walls were preheated at 100 °C for 2 h and, all of the delivery lines were heated at 120 °C to prevent precursor condensation. The reactor chamber pressure was set to 20 Pa. The metalorganic precursor trimethyl-aluminum $Al(CH_3)_3$ (TMA, from Strem Chemicals inc.), kept at room temperature (RT), and $O_2$-plasma were used as aluminum and oxygen sources, respectively. Nitrogen ($N_2$) gas, at a flow rate of 40 sccm, was used as a carrier for the TMA precursor and for the purging step. A radio frequency (RF—13.56 MHz) remote plasma source at a power of 200 W was used to create oxygen plasma. The ALD cycle consisted of a TMA pulse (80 ms) followed by a 2 s of plasma exposure. Two purging steps with nitrogen (99.9995%) for 3 and 1 s, respectively, were needed to remove any unreacted precursors (total time of each cycle equal to 6.08 s). The nominal growth rate per cycle, determined to be 0.06 nm, led to the repetition of the process for 100 cycles at a deposition temperature of 100 °C (around 6 nm). This growth rate was estimated by measuring the thickness of a film of $Al_2O_3$ deposited on a silicon substrate under similar conditions, using a spectroscopic ellipsometer (SE) J. A. Woollam M-2000 system in the Vis/NIR range (450−850 nm) at three angles of incidence (70, 75, 80°).

The model used to fit the SE data consisted of three layers: silicon for substrate,[37] native silicon oxide,[38] and dielectrics as top layer. In a simplified picture, a Cauchy model was used for fitting $\psi$ ($\lambda$) and $\Delta$ ($\lambda$) acquired for $Al_2O_3$ layers, as generally used for ALD oxides.[39] Each fit was considered reliable when the mean square error (MSE),


https://doi.org/10.1021/acsanm.4c01827
ACS Appl. Nano Mater. 2024, 7, 18724−18736

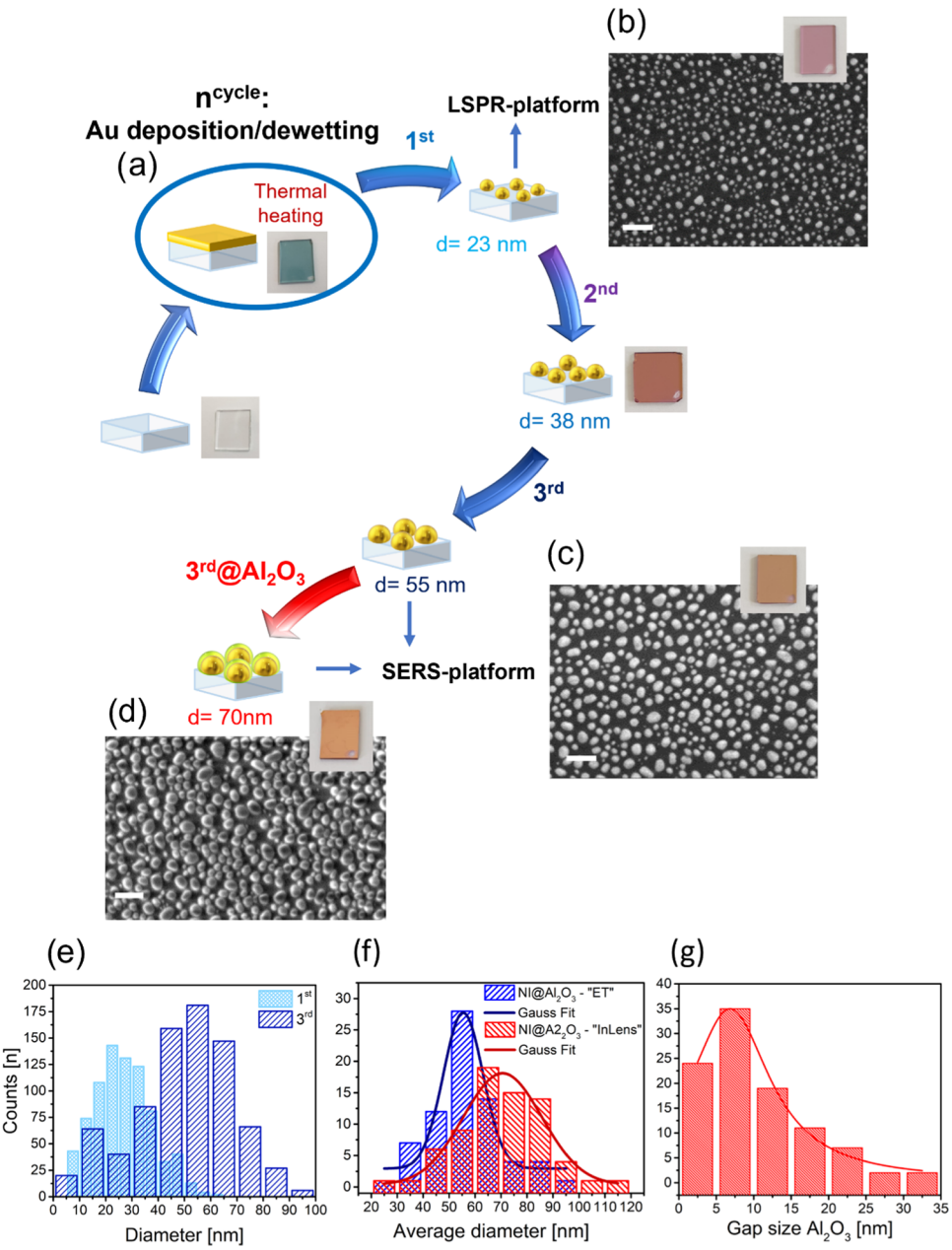


**Figure 1.** (a) Schematic illustration of Au NIs after three consecutive gold deposition/thermal dewetting cycles and alumina deposition. The images of the glass slides covered by Au NIs, after each fabrication step, show the color changes due to the different LSPRs. Scanning electron microscopy (SEM) images of gold NIs after different deposition/dewetting steps: 1st (b) and 3rd cycles (c) and after alumina deposition ((d)—3rd@$Al_2O_3$), scale bar equal to 200 nm, respectively. The average diameter was estimated using "ImageJ" software before (e) and after (f) $Al_2O_3$ deposition on NIs. The $Al_2O_3$-coated sample was analyzed with two different detectors of secondary electrons: the ET detector selectively detects gold material at the nanoisland scale; conversely, the InLens detector reveals fine structures invisible to the ET detector, allowing visualization of the alumina shell. (g) Distribution of gap sizes among the $Al_2O_3$-coated nanoislands. The histograms of parts (f) and (g) were obtained using 71 and 100 samples, respectively. Gaussian fits were applied for interpolation, resulting in *R*-squared values of 0.9642 (ET) and 0.9443 (InLens) for (f) and 0.98105 for (g).

defined as mean of the square of the difference between experimental and estimated values, was below 5.

**2.3. Morphological Characterization.** Surface topography of gold and gold/alumina NIs was recorded by using a Zeiss Merlin scanning electron microscope at low energy (5 keV). The sample with $Al_2O_3$ was analyzed with two different detectors of secondary electron: "Everhart-Thornley" (ET) detector enables to detect only gold material at the nanoisland scale; conversely, the "InLens" detects fine structures that are invisible to ET detector; hence it is possible to appreciate also the alumina shell. The images were analyzed by using the open-source software "ImageJ" to measure the size and shape distribution of the NIs.

**2.4. Surface Wettability and Contact Angle Measurements.** Static contact angle measurements were performed at room temperature (RT) using a CAM 200 instrument (KSV Instruments Ltd., Finland) by depositing 25 $\mu$L of water or 10% FBS in water (with or without DOX) onto Au NIs. Each data point represents the average of the left and right contact angles measured in three different regions of the surface. The error bars represent the standard deviation.


https://doi.org/10.1021/acsanm.4c01827
ACS Appl. Nano Mater. 2024, 7, 18724−18736

**2.5. Optical Characterization of the Gold Nanoislands.** The optical characterization of the interaction between Au NIs and DOX was carried out by using two different optical setups.

The first homemade optical setup, placed at the CNR Institute of Nanotechnology (Italy), was used for the optical measurements with DOX dissolved in ultrapure water and 10% FBS. Each spectrum is the average of 20 measurements. A glass slide was used as the blank. The transmission/extinction measure was performed in solution-like conditions: 25 $\mu$L of DOX solution (dissolved either in water or 10% FBS) was dropped onto the NIs and, after 1 h incubation, a glass coverslip was placed onto the sample prior to be measured. The control sample was prepared by dropping 25 $\mu$L of the solvent (either water or 10% FBS) onto the glass slide and placing the glass coverslip after the incubation time.

To set the titration curve, 12 different samples with an average LSPR peak of (552.8 ± 0.8) nm and a relative standard deviation of 0.15% were used.

The second setup, a Shimadzu UV-2700 spectrophotometer, located at the Institute of Biophysics of the Ministry of Science and Education (Azerbaijan), was used for optical measurements (transmission/extinction) of the human serum samples from patients who had undergone DOX administration. Human serum samples were collected 1 h after the administration of DOX (110 mg) to patients.

Untreated glass was used as a blank in the spectrophotometric measurements, while healthy human serum blood was used as a control sample. As already described, 25 $\mu$L of human serum was deposited onto NIs and incubated for 1 h on a shaker in the dark. Soon after, the Au NIs-glass samples were slowly dried at room temperature and measured.

**2.6. Estimation of DOX Binding to Au NIs.** In DOX titration measurements, the shift of the extinction maxima was used to estimate the dissociation constant ($K_d$). The experimental data were fit to the following well-known Hill−Langmuir equation:

$$\Delta\lambda = \frac{\Delta\lambda_{max} \times [DOX_T]^n}{K_d + [DOX_T]^n} + c$$

where $DOX_T$ is the titrated total concentration, $n$ is the Hill coefficient suggesting the cooperativity of binding, and $\Delta\lambda_{max}$ corresponds to the maximum shift of the extinction maxima during titration experiments. In this equation, the $DOX_T \sim DOX_{free}$ approximation is used, which is applicable because the concentration of DOX significantly exceeds that of Au NIs on the surface of the glass; the $c$ is constant to account for the vertical shift of baseline. $K_d = (K_A)^n$, and $K_A$ is the ligand concentration that produces half occupation of the binding sites. The $K_d$ values for DOX in water and FBS were estimated by global fitting the titration data to this equation with the nonlinear least-squares method. The values of $\Delta\lambda_{max}$ and $n$ are global parameters in the fitting procedure.

**2.7. SERS Measurements with Au/$Al_2O_3$ NIs.** SERS measurements were carried out by using a Horiba Xplora Micro-Raman instrument equipped with a 532 nm laser. Spectra were acquired with a laser power of 0.125 mW $cm^{-2}$ and a 10× objective. Ten $\mu$L of DOX solution at different molar concentrations (either in water or 10% FBS) were drop-casted on the Au/$Al_2O_3$ NIs and left at 4 °C overnight. Before analysis, the DOX was rehydrated with 10 $\mu$L of ultrapure water. All of the measurements were performed in the wet state. To quantify the enhancement achieved by the addition of the $Al_2O_3$ layer, we calculated the enhancement factor (EF) for the investigated substrates using the formula:

$$EF = \frac{I_{SERS}}{I_{Raman}} \times \frac{N_{Raman}}{N_{SERS}}$$

where $I_{SERS}$ represents the intensity of the SERS signal at 470 $cm^{-1}$ recorded for the substrate with and without $Al_2O_3$ substrates, $I_{Raman}$ represents the intensity of the SERS signal at 470 $cm^{-1}$ in the spectrum of the sample used as the control (glass@$Al_2O_3$), $N_{SERS}$ and $N_{Raman}$ represent the number of analyzed molecules both in SERS and Raman conditions, considering the volume (10 $\mu$L), the molar concentration, and Avogadro's number ($N_A$).

**2.8. Reusability of the Devices.** To assay the reusability of the sensor, after each measurement, the samples were washed thoroughly with water, and the wavelength of the extinction peak was recorded. The obtained value was set as the starting NI extinction peak and used to estimate the relative shift of the band position in the next measurement. The same sample was reused 2−3 times.

## 3. RESULTS AND DISCUSSION

**3.1. Fabrication of Au NIs and Au/$Al_2O_3$ NIs-Based Sensor Architectures.** Two types of gold nanostructure-based sensor architectures have been fabricated and applied to drug detection in either water, bovine serum, or human serum: a localized surface plasmon resonance (LSPR)-based device made of Au NIs for quick and inexpensive optical detection (Table S1 in Supporting Information (SI)), and a surface-enhanced Raman scattering (SERS)-based sensor made of Au/$Al_2O_3$ NIs (core/shell nanostructures) for more sensitive measurements.

Indeed, the latter represents the evolution of the simple Au NIs with the aim of improving the detection sensitivity at the expense of a reduced speed of the readout. The fabrication steps of the devices are schematically illustrated in Figure 1.

As reported in the literature,[40] the thickness of Au film and the annealing temperature are crucial parameters that affect the optical properties of the Au NIs. In the present study, the furnace temperature is chosen that is close to the glass softening point to improve the poor adhesion between gold and the glass substrate without using titanium or chromium as adhesion layers. After the annealing process, gold and glass show different cooling times. Therefore, while the glass remains moldable, the Au film becomes solid and penetrates into the glass.[41] As proof of embedding, the SEM image in Figure S1a displays the cross section of gold NIs and the glass substrate after etching by dipping into iodine tincture; the sinking depth depends on the annealing temperature and is achieved with an annealing time of at least 3 h (Figure S1b). This crucial feature, requiring a long annealing time, opens up the prospect of employing the sensor across a wide spectrum of biological fluids without causing NIs lift off or aggregation. Furthermore, it enables the utilization of an optically transparent, chemically inert, cost-effective, and easily accessible substrate. The gold thickness was chosen to be thinner than the percolation threshold (5 nm),[40,42] resulting in a structure consisting of alternating gold and void regions. During annealing, these voids enlarge and the thin film undergoes dewetting, retracting to form distinct gold NIs.[43,44] Additionally, gold atoms on the film surface can diffuse and merge, leading to the growth of larger nanoparticles through a process of Ostwald ripening.[21] Random imperfections or surface irregularities serve as nucleation sites for gold atom adhesion. The formation of the gold nanostructures thus occurs through nucleation and coalescence, with the "center to center" (c-to-c) distance between two adjacent NIs depending on the thickness of the deposited Au.[42]

The optical spectrum of the nanoislands exhibits the typical plasmonic peak in the visible region, dominated by the fundamental dipole resonance according to Mie theory and localized at about (552 ± 2) nm, as shown in Figure S2a. This absorption peak is consistent with the average size of Au NIs (25 nm).[42,45]

Furthermore, to realize high efficiency SERS-active structures, the fabrication process of NIs was modified: the deposition/dewetting cycle was repeated two more times (a 5


https://doi.org/10.1021/acsanm.4c01827
ACS Appl. Nano Mater. 2024, 7, 18724−18736

nm thick Au layer was added at each step—Figure 1a); the starting gold film acts as a seed for subsequent nucleation, leading to the lateral enlargement of the NIs and a reduction in the interstitial gap spacing between them (Figure 1e).[46] Consequentially, after three Au deposition/thermal dewetting cycles (3rd), the Au NIs color changes to a pink-gold color and has a mirror-like surface. These color variations are obviously correlated to the increasing size of the NIs and thus to the variation of the plasmon peak wavelength. The pictures of the NIs, after each fabrication step, show the color variation of the surface (Figure 1).

By increasing the number of cycles, the NIs size doubles from an average diameter of (23 ± 10) to (55 ± 10) nm after 3 cycles, as displayed in Figure 1b,c, and Table 1 where the

**Table 1. Extinction Intensity and Diameter Enlargement After Each Fabrication Step of Au NIs and Au/$Al_2O_3$ NIs**

| cycle [$n$] | $\Delta I$ [%] | $\Delta d$ [%] | th $Al_2O_3$ [nm] | c-to-c [nm] |
|---|---|---|---|---|
| 1st | 0 | 0 | / | 60 ± 15 |
| 2nd | 13 | 65 | / | 62 ± 16 |
| 3rd | 23 | 140 | / | 65 ± 12 |
| 3rd@$Al_2O_3$ | 26 | 200 | 7 ± 5 | 65 ± 20 |

percentage increase of the diameter is reported. However, the center-to-center distance between neighboring islands $g_0$ is essentially unchanged (Figure 2a), thus demonstrating the radial growth of the structures after each cycle. Hence, the average gap defined as $g = (g_0 - 2r)$, where $r$ is the average radius, decreases from around (40 ± 10) to (7 ± 5) nm, confirming that, upon repeated cycles, the NIs occupy a larger area on the glass substrate with the Au-fill factor becoming greater than the initial one, from 22% (after 1 cycle) to 36% (after 3 cycles). To further enhance the electromagnetic (EM) field between NIs, as experimentally demonstrated in our previous work,[47,48] we fabricated Au/dielectric-core/shell NIs using a large refractive index dielectric coating. This additional fabrication step was introduced to enhance the plasmonic hot spots between neighboring Au NIs by leveraging the dielectric Mie resonances that occur in plasmonically coupled NPs.[47,49−51] We evaluated $SiO_2$ and $Al_2O_3$ as potential coating materials, with $Al_2O_3$ demonstrating superior dielectric properties. This resulted in a more pronounced LSPR shift, approximately 10 nm for $Al_2O_3$ compared to 3−5 nm for $SiO_2$ (Figure S3), and enhanced local electromagnetic field intensities.[47,48] The effective coating of Au nanoparticles (Au NP) by $Al_2O_3$ is facilitated by a strong bond with the gold atoms, characterized by a binding energy of 0.79 eV. This bonding mechanism is attributed to charge transfer between the $Al_2O_3$ and Au NP.[52] Acting as an insulating spacing layer, $Al_2O_3$ plays a crucial role in modulating electronic and energy communication among adjacent Au NIs.[53] Furthermore, $Al_2O_3$ offers excellent chemical stability, which is essential for maintaining the integrity of the plasmonic structure over time, particularly in biological environments.[34]

To this aim, the fabrication process was completed by plasma-enhanced atomic layer deposition (PE-ALD) of $Al_2O_3$ thin films over the NIs. $Al_2O_3$ provides a high refractive index in the visible region, where it is nearly transparent (zero loss). Notably, the ALD process provides a highly precise control of the thickness, an extremely low contamination content, excellent uniformity, and conformality on complex three-dimensional (3D) structures and consequently allows one to finely control the gap narrowing between Au NIs.

An enhancement of the plasmonic hot spots at the nanogaps could also be attained without a dielectric layer, employing additional Au deposition/dewetting steps. However, these steps are costly and may produce a detrimental electron

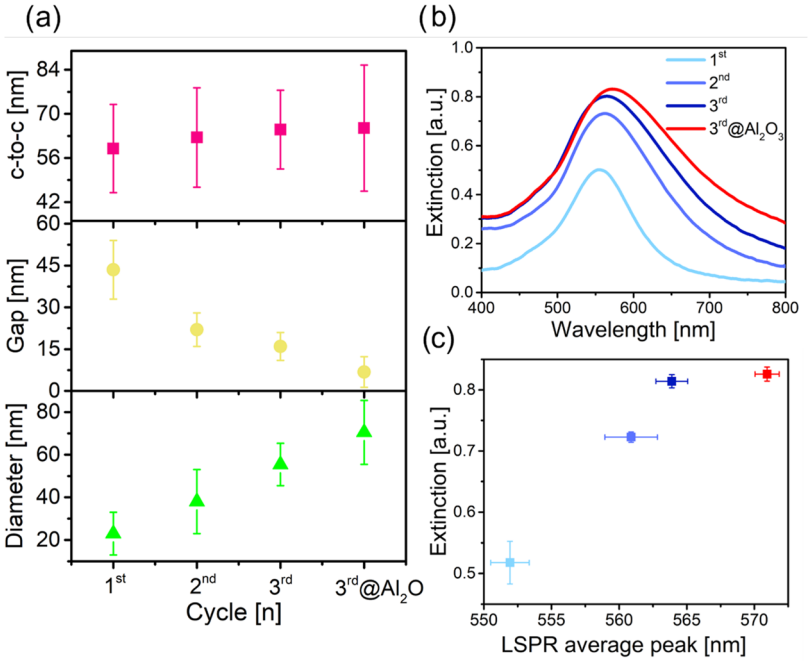


**Figure 2.** (a) The average diameter, gap, and center-to-center distance of the NIs after each cycle. All averages are taken from ca. 100 NIs, and data represent the mean ± standard deviation of 20 samples fabricated in various deposition/dewetting cycles. (b) Extinction spectra of gold NIs obtained after the 1st, the 2nd, and the 3rd cycles, and after alumina deposition, respectively. (c) Average intensity and spectral position of the extinction peaks assessed on more than 20 samples for each fabrication cycle.



https://doi.org/10.1021/acsanm.4c01827
ACS Appl. Nano Mater. 2024, 7, 18724−18736

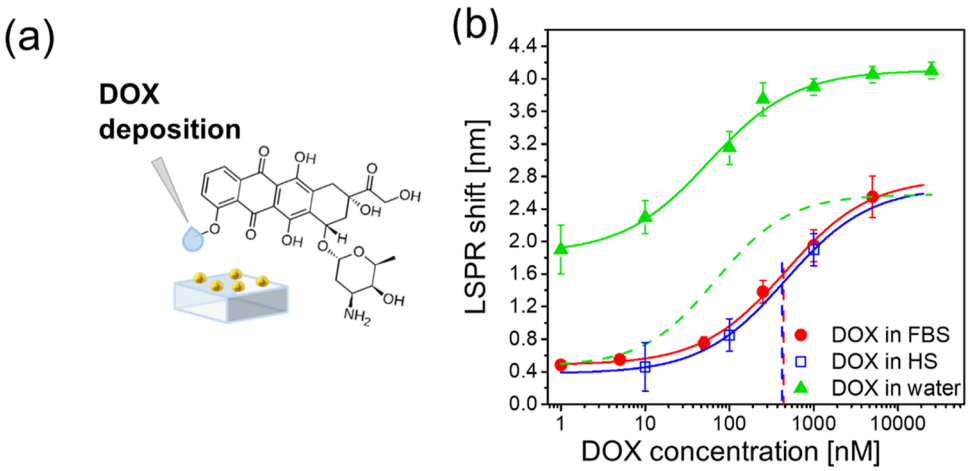


**Figure 3.** Schematic illustration of (a) one gold deposition/dewetting cycle followed by DOX incubation; (b) DOX binding to the Au NIs on the glass surface in water, 10% FBS, and 10% HS. Triangle, circle, and open square symbols show the concentration-dependent shifts, respectively. Solid lines are the best fit obtained from the binding formula (see Section 2.6). The binding curve for DOX in water is vertically shifted (green dashed line) to better visualize differences in the $K_A$ values. $K_A$ values are represented in the panel as vertical dashed lines and refer to the different DOX_Au NIs systems. All measurements are registered five times, and data represent the mean ± standard deviation of 10 samples fabricated in various deposition/dewetting cycles. Hill equation fits were applied to interpolate the experimental data, resulting in similar *R*-squared values of 0.996 for all three fluids.

tunneling between metallic NPs in the case of a sub-1 nm gap.[54] Top-view SEM images in Figure 1c,d show the morphologies of the 3rd and 3rd@$Al_2O_3$ NIs. An in-depth analysis, based on SEM, was performed on Au@$Al_2O_3$ samples to evaluate the alumina thickness after 100 ALD cycles. Indeed, by analyzing the same sample through two different secondary electron detectors, as ET and InLens, it is possible to distinguish the diameter of the core (composed of gold) and the core−shell as illustrated in Figure 1d.

The image analysis revealed a further increase in the NIs' diameter of approximately 15 nm (Figure 1f). Therefore, an average shell of about 7.5 nm encapsulates the gold nanostructures. This finding is in excellent agreement with the nominal value mentioned in the Methods section. As shown in Figure 2a, the NIs diameter and the average interstitial gap have an opposing trend: while the diameter follows linear growth, the gap decreases at each step up to 7 nm after $Al_2O_3$ deposition. As shown in the histogram of Figure 1g, a mere 24% of the nanogaps exhibit a width spanning between 0 and 5 nm, thus contributing to the generation of "hot spots" (regions of concentrated electromagnetic field intensity). This contribution significantly diminishes between 6 and 10 nm.

Figure 2b shows the progressive shift toward NIR wavelengths of the Au Nis' extinction peaks after each deposition/dewetting step and alumina deposition.

Furthermore, the lateral enlargement of the NIs decreases the transparency of the film (Figure 2b), thus resulting in a rigid vertical shift of the extinction spectra to higher values.

To accurately evaluate the increase in the extinction intensity by the number of fabrication cycles, all spectra were normalized to compensate for the vertical shift, setting the starting point at zero.

Hence, the extinction ratio, named % $\Delta I$ and defined as $\frac{(I_{max_i} - I_{max_1})}{I_{max_1}}$ (where $I_{max_i}$ is the maximum value of average extinction with $i$ = 1−4 is the cycle number), was reported in Table 1, along with the percentage variation of diameter.

As can be noted in Table 1, an extinction increase (% $\Delta I$) was observed by repeating the deposition/dewetting steps and after the deposition of a 7.5 nm thick $Al_2O_3$ layer (about 3%) due to dielectric Mie resonances, as previously mentioned.[47,50] Table 1 also reports the enlargement of the NIs diameter (% $\Delta d$) at each cycle.

To evaluate the repeatability of the fabrication process, a comparative analysis of more than 20 samples per fabrication cycle, produced at various times, was performed to obtain the average intensity and spectral position of the plasmonic resonances.

As displayed in Figure 2c, the error bars decrease with increasing fabrication cycles, thus demonstrating greater uniformity and reduced variability in the size of the NIs.

Finally, the stability of the plasmonic devices was investigated. The samples were stored in the dark at room temperature and exposed to ambient air for several months. Figure S4a shows the aging behavior of the devices after 1, 6, and 12 months. The recorded LSPR shift in the graph is around 1 nm, thus guaranteeing the long-term stability and functionality of the platform. Additionally, the stability in a humid environment was analyzed. Three samples, with similar plasmonic peaks, were immersed in deionized (DI) water and measured after 1, 3, and 24 h. The measured shift is around 0.6 nm, as displayed in Figure S4b.

**3.2. LSPR-Based Detection of DOX by Au NIs.** After the optical and morphological characterization, the NIs were evaluated as sensing structures of DOX, whose absorbance spectrum exhibits a peak at approximately 485 nm (Figure S2). To assess the sensitivity of the device obtained after one deposition/thermal dewetting cycle, three sets of optical measurements were performed: one using DOX dissolved in ultrapure water, another with DOX in 10% FBS, and the third using 10% HS collected from patients who had previously been injected with the drug.

Specifically, 25 $\mu$L of the DOX solutions (at concentrations ranging from 1 nM to 25 $\mu$M) were dropped onto the Au NIs without the use of any binding moiety or linking molecule, and after incubation at RT in the dark (Figure 3a), the LSPR


https://doi.org/10.1021/acsanm.4c01827
ACS Appl. Nano Mater. 2024, 7, 18724−18736

spectra were recorded. The shifts of the plasmon peaks were attributed to the interaction between DOX and NIs, while the magnitude of the plasmon shift depended on the bond drug concentration.

Initially, three incubation times were considered (30 min, 1 h, and 3 h): 30 min was insufficient to establish stable interactions between the NIs and the drug, as evidenced by the absence of a plasmon resonance shift (data not shown), while after 3 h, the recorded LSPR spectra were indistinguishable from those collected after 1 h. Therefore, a 1 h incubation time, which is consistent with the clinical analysis standard duration, was chosen for all of the measurements. In each experiment, as depicted in Figure 3b, either ultrapure water, fetal bovine serum, or human serum was employed as control solution. The Nis' plasmonic peak value is recorded in air at the beginning of the experiment. Subsequently, the nanoislands were immersed in the respective control solution, without DOX, for 1 h and the new plasmonic peak was recorded. The plasmon shift upon dipping in the control solution, along with the standard deviation, is 0.5−0.9 nm for water, 2.0 nm for FBS, and 2.2 nm for HS (both 1:10 diluted in water) (Table S2 in SI). Furthermore, upon the addition of DOX (in either water or 10% FBS), the plasmon peak exhibited a concentration-dependent red shift (Figure S5). The shift was estimated by subtracting the LSPR measurement of each control (either FBS, HS, or water) from the LSPR measurements acquired at various DOX concentrations.

The area-normalized spectra of DOX show an isosbestic point at 575.0 and 572.0 nm in water and serum, respectively (Figure S5a,b). The isosbestic point in titration experiments indicates that only two species are present (free Au NIs and Au NIs-DOX complexes), and their concentrations change in a stoichiometric manner. The variation of the isosbestic point might be attributed to the difference in the initial extinction maximum wavelength.

Thus, the dependence of the extinction maximum wavelength on the drug concentration can be exploited to determine the DOX concentration required to saturate the binding sites of Au NIs. The binding curves are presented in Figure 3b, where the concentration is plotted on a logarithmic scale. The DOX_water system (triangle points) exhibits a typical sigmoidal shape, with the LSPR shift increasing as the DOX concentration increases from 1 nM to 25 $\mu$M.

At low DOX concentrations (from 1 to 10 nM), the device displays poor responsiveness, but at concentrations above 10 nM, the plasmon shifts increase linearly until saturation is reached in the 1−5 $\mu$M range. The DOX_10% FBS system (solid circle points) and DOX_10% HS (open square points) display similar behavior.

To investigate whether the saturation regime is related to the occupation of all of the available binding sites on the sensor structure, a theoretical estimation (as detailed in the Supporting Information) indicates that a DOX concentration of around 500 nM is sufficient to saturate all of the binding sites. This theoretical prediction aligns with the binding curves of the DOX_water system (Figure 3b), where the linear trend no longer persists at concentrations greater than 250 nM, and at a concentration of 500 nM, 88% of the binding sites are occupied, as depicted in the Hill function simulation of Figure S6. This behavior is characteristic of sensors having a finite surface area where DOX forms a secondary layer following the saturation of the NIs' surface.[55]

A similar trend was observed in the DOX_10% FBS and DOX_10% HS systems, where the presence of serum proteins shifts the titration curves and the dissociation constant $K_d$ (defined as $K_d = (K_A)^n$, where $K_A$ is the ligand concentration that produces half occupation of the binding sites, and $n$ is the Hill coefficient suggesting the cooperativity of binding) toward the NIR (Figure 3b). Due to the low molecular weight of DOX, a small shift (around 2 nm) of the LSPR accounts for the detectable concentration range of the sensor before the saturation region.[56] In the linear region (logarithmic scale), the LSPR shift can be fitted with the linear function whose slope represents the LSPR sensor sensitivity ($S$). Consequently, the sensitivity can be used to calculate both the limit of detection (LOD) and the limit of quantification (LOQ), which are two crucial parameters of the LSPR-based analytical method. When DOX is dissolved in water, the estimated LOD is about 1 nM, that is in good agreement with the coefficient of determination $R^2 = 0.9664$, while the LOQ is 3 nM. A similar trend is obtained when DOX is dissolved in 10% FBS at various concentrations (Figure 3b, solid circle dots). The estimated LOD is around 16 nM ($R^2 = 0.9553$), a value higher than that observed in DOX_water NIs, likely due to the inference of the serum proteins that interact with the drug, de facto reducing the detectable drug concentration.[57]

The experimental data were fitted to the Hill equation ($R^2 = 0.9963$), yielding apparent $K_A$ values of (57 ± 14) and (439 ± 89) nM for DOX-Au NIs in water and 10% FBS, respectively, as shown in Figure 3b. The corresponding apparent dissociation constant ($K_d$) values were calculated to be (35 ± 8) and (205 ± 52) nM, respectively. These $K_d$ values suggest that DOX-Au NIs exhibit avid complex formation in both water and FBS.

However, the affinity of DOX for Au NIs decreases significantly in the presence of 10% FBS. Nevertheless, a dissociation constant of (205 ± 52) nM is still considered indicative of a strong binding. Analyzing the global fitting of the association data to the Hill−Langmuir equation provided valuable insights on the estimated global parameters of $n$ (0.87 ± 0.05) and $\Delta\lambda_{max}$ (2.25 ± 0.03) nm. Indeed, the low standard deviations suggest that the binding properties of the Au NIs are not significantly altered in the presence of 10% FBS and the estimated Hill coefficient indicates minimal negative cooperativity to the binding.

Despite the low molecular weight of DOX, the LOD of the sensor system is a few nanometers. Unlike free-standing nanoparticles, which are completely surrounded by either air or drug solution, nanoislands are partially embedded in glass, whose dielectric constant is higher than air. As a result, the effective surrounding dielectric constant of the partially embedded Au NIs is higher than that of fully air-exposed nanoparticles, leading to a stronger electric field and enhanced sensitivity, as theoretically demonstrated in refs 58,59.

Further experimental evidence of the interaction between DOX in 10% FBS and NIs is provided by the variation of the contact angle of the sensor surface upon variation of the DOX concentration (Figure S7). The observed trend is consistent with that of the Langmuir isotherm: as the concentration of DOX increases, the binding sites (Au NI surfaces) are progressively saturated leading to a gradual decrease in surface hydrophilicity from 36.6 to 52.5°. On the other hand, without DOX, the surface of the sensor is hydrophilic due to the presence of glass, as the Au NIs coverage is around 20% of the whole surface.



https://doi.org/10.1021/acsanm.4c01827
ACS Appl. Nano Mater. 2024, 7, 18724−18736

The experimental data of the contact angle measurements were fitted to the Hill equation ($R^2$ = 0.9982), resulting in an apparent $K_A$ value of (472 ± 65) nM (Figure S7, vertical dashed line). The derived global parameter $n$ (0.81 ± 0.04) and apparent $K_d$ values (150 ± 33) nM, respectively, are in good agreement with the experimental data of Figure 3b. Thus, the surface of Au NIs became more hydrophobic upon chemical interaction with DOX without any functionalization of the sensor surface with organic linkers.

Next, the clinical feasibility of the Au NIs sensor was assessed by testing serum samples from cancer patients who underwent DOX chemotherapy. The experimental measurements were conducted 1 h after drug administration; the serum samples from patients who did not receive DOX was analyzed as control samples. A calibration curve was established by preparing solutions of DOX at various concentrations (1, 10, 100, and 1000 nM) in 10% HS, and measuring the maximum shift of the excitation peak. The HS titration points were compared to the titration curve obtained with 10% FBS. The results, as shown in Figure 3b, demonstrate remarkable similarity between the two sets of data. The shift recorded at 1 nM DOX in 10% HS falls within the error margin of the control sample (10% HS in water). Global analysis of the data revealed that the largest shift and the dissociation constant ($K_d$) remained largely unchanged, while the cooperativity constant decreased from 1 to 0.9, indicating mainly non-cooperative binding. Despite the different types of serum, a LOD of 16 nM was estimated, comparable to that of DOX samples dissolved in 10% FBS.

Subsequently, the serum samples from cancer patients were diluted 1:10 to align the calibration curves of the HS and incubated with the Au NIs for 1 h. The recorded plasmon shift (around 2.2 nm) was plotted on the HS Hill−Langmuir curve to determine the corresponding DOX concentration of the patient serum, as shown in Figure S8. A DOX concentration equal to 77.5 nM was obtained with an asymmetric error in the range reported in Figure S8.

Since the measured sample was diluted 1:10, the initial concentration of DOX in blood should be 10 times higher, yielding a value close to 775 nM, which corresponds to approximately 420 ng $mL^{-1}$. This finding is in agreement with the values reported in the literature for cancer patients who received approximately 110 mg of doxorubicin as part of their therapy regimen.[60,61]

As a crucial validation step, the final measurement of the LSPR shift, shown in Figure 4, was performed in undiluted blood serum, resulting in a discernible shift of 2.6 nm compared to the control sample without DOX.

These data highlight the potential translation of this platform to clinical diagnostics, enabling rapid determination of circulating DOX concentrations, and aiding in optimizing treatment strategies while minimizing adverse effects in treated patients.[62] Importantly, the presence of the isosbestic point, both in water (575 nm) and 10% FBS (572 nm), further corroborates the accuracy of the detection. This remarkable consistency, with an error of approximately 1.5 nm and a negligible relative standard deviation of 0.26% (Figure 4), confirms the robustness and reliability of the sensor platform.

To evaluate the reusability of the devices, the nanostructures were washed and soaked in ultrapure water for 1 h followed by air drying. Optical measurements confirmed the complete removal of DOX from the gold NIs surface, as evidenced by a shift of the plasmon peak of less than 0.05% (Figure S9).

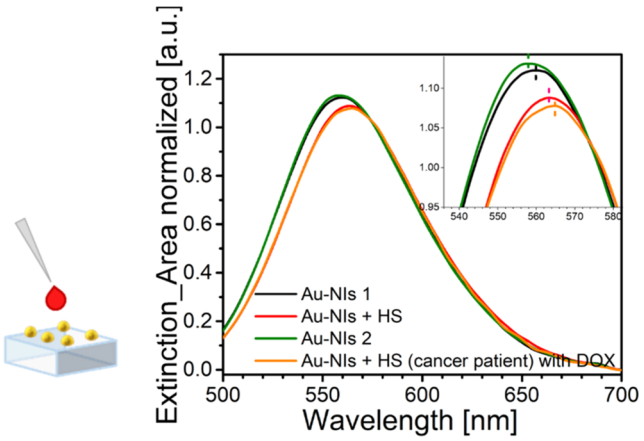


**Figure 4.** Extinction spectra of Au NIs after incubation with undiluted human serum (HS) blood coming from cancer patients administrated with DOX; the inset shows a zoom of the LSPR shift. The numbers 1 and 2 refer to reusability of the device. The isosbestic point is localized at 574 nm.

However, after three reuse tests, the devices could no longer be used, likely due to the adsorption of molecules that could not be removed upon thorough washing. Indeed, the plasmon peak did not shift anymore after the washing test (both the intensity and wavelength).

Finally, the bubble-like structures observed during SEM imaging (Figure S10) indicate the formation of an organic layer, sensitive to the electron beam, above the gold nanoislands after the deposition of DOX (100 nM), confirming the presence of the drug molecules. These structures are likely due to the interaction between the electron beam and the organic molecules present in the layer.

**3.3. SERS-Based Detection of DOX on Au NIs and Au/$Al_2O_3$ NIs.** The absorbance spectrum of DOX exhibits a prominent peak at approximately 485 nm, making it readily excitable by a green laser operating at a wavelength of 532 nm. As shown in Figure S2a, the incident laser radiation resonates with the localized surface plasmon resonance (LSPR) of the gold nanoparticles (Au NIs). This coherent interaction between the incident electric field and the dipolar electric field induced by the LSPR oscillations results in a redistribution and amplification of the electric field intensity in the vicinity of the nanostructure.

Initially, when a highly concentrated (23 $\mu$M) solution of DOX was applied onto a glass substrate solely coated with the alumina layer (control sample without NIs; Figure S11a), an exceptionally weak Raman signal was detected.

Subsequently, NIs substrates (1st, 2nd, and 3rd cycles) were employed, and the SERS effect was assessed following incubation with 10 nM DOX dissolved in water; unfortunately, weak signals were observed (Figure S11b), but were still detectable for all of the samples. To improve the platform performance, the substrate having the highest count number (3rd cycle, Figure S11b) was coated with aluminum oxide to enhance the DOX Raman mode.

This 3rd@$Al_2O_3$ sample exhibited a remarkable SERS effect (red spectrum), as displayed in Figure S11b. To validate this performance, measurements were performed with aqueous solutions of DOX in the concentration range 0.1−100 nM (Figure 5a). Furthermore, the SERS measurements were carried out with Au NIs (3rd) incubated with DOX in the 1−10,000 nM range (Figure S11c) and with Au NIs 1st upon


https://doi.org/10.1021/acsanm.4c01827
ACS Appl. Nano Mater. 2024, 7, 18724−18736

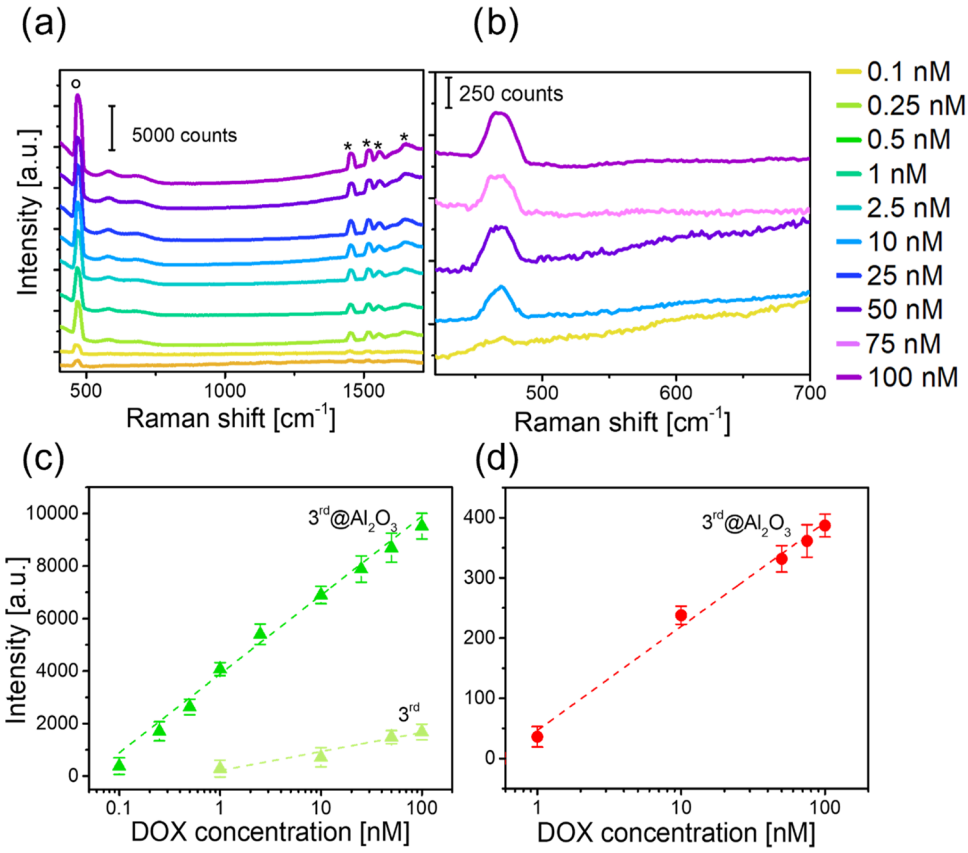


**Figure 5.** SERS spectra (a) of water solutions of DOX in 0.1−100 nM concentration range and (b) of 10% FBS solutions of DOX in 1−100 nM concentration range on 3rd@$Al_2O_3$ substrate. Titration curve (in logarithmic scale) obtained at 470 cm$^{-1}$ Raman peak intensity in the case of the 3rd and 3rd@$Al_2O_3$ substrate in water (c), and in the case of (d) the 3rd@$Al_2O_3$ substrate in 10% FBS is reported. $R^2$ is 0.97 for both curves reported in (c) and 0.98 for (d). All average data represent the mean ± standard deviation of 10 samples fabricated in various deposition/dewetting cycles.

incubation with DOX in the 1−100 nM concentration range (Figure S11d), respectively.

The spectra were recorded within the 400−1700 cm$^{-1}$ range since the most characteristic signals of DOX are in the region of the conjugated aromatic rings of the molecule. Indeed, Raman modes, denoted by the asterisks in Figure 5a, correspond to typical vibrations of the DOX molecule.[28]

The most prominent signal, located at 470 cm$^{-1}$ (open circle dot), is a composite signal arising from the in-plane bending of C═O and C−C−O groups;[63−67] these groups are likely involved in the interaction with the substrate, as evidenced by the significant enhancement of the intensity, consistent with literature findings.[68] Additionally, the signals within the 1350−1600 cm$^{-1}$ range predominantly originate from stretching vibrations of the aromatic rings and CCOCH in-plane bending of the chromophore of DOX.[63] Other contributions, typically present in the DOX spectrum and attributed to skeletal deformations or ring breath, are conspicuously absent. This observation suggests a preferential conformation of the molecules with the longer axis parallel to the substrate, a consistent feature across all investigated samples.[68]

It is crucial to highlight that although the 1st, 3rd, and 3rd@$Al_2O_3$ substrates enabled the detection of DOX SERS signals at low concentrations, the SERS intensity attained with the 3rd@$Al_2O_3$ substrate was notably superior. Specifically, the EF was calculated, as reported in the Section 2.7, for the 3rd and 3rd@$Al_2O_3$ samples and we obtained, for the latter sample, an EF of $10^6$ which is 3 orders of magnitude higher than the value calculated for the third sample.

Despite this, both 3rd (Figure 5c) and 3rd@$Al_2O_3$ (Figure 5c) displayed a linear response (in logarithmic scale, $R^2$ > 0.97). Intriguingly, an experimental limit of detection (LOD) of 1 nM and 100 pM was determined within the investigated concentration range, respectively. Significantly, these two substrates exhibit a distinct difference in sensitivity, underscoring the critical role of engineering Au/$Al_2O_3$ NIs in the development of an ultrasensitive SERS-based sensor.

Actually, $Al_2O_3$ acts as an insulating spacing layer, crucial for modulating electronic and energy communication among adjacent Au NIs and between doxorubicin molecules and gold, preventing the quenching of the SERS effect due to tight connections.[53] Additionally, the application of LSPR-based SERS is often limited by heat generated from severe loss in interband transitions damaging molecules and modifying molecule−NP interactions.[69,70] The laser excitation at 532 nm (commonly the absorption-rich part) corresponds to 87% of the absorbance peak for the first sample, while it decreases for the 3rd@$Al_2O_3$ sample due to the peak position shift, resulting in lower plasmonic heat generation (Figure S2a,b).

To the best of our knowledge, a 100 pM experimental LOD has not been previously reported for DOX in SERS-based and label-free sensors. It can be eventually argued that $Al_2O_3$ serves as both an insulating layer and a molecular spacer, optimizing the distance between DOX and NIs surfaces to tune the electronic and energetic communication among DOX


https://doi.org/10.1021/acsanm.4c01827
ACS Appl. Nano Mater. 2024, 7, 18724−18736

molecules and NIs. Thus, $Al_2O_3$ ensures an optimal plasmonic coupling and, thus, the enhancement of the electromagnetic field interacting with the DOX molecules upon 532 nm laser irradiation.[47,53,71] These observations demonstrate that the synergistic combination of the two materials represents the optimal structural configuration for the SERS-based analysis.

It is noteworthy that all of the measurements were carried out in the wet state, involving the rehydrating DOX being adsorbed onto the surface. In the dried state, no signal was detected. Water solvation appears crucial for maintaining the intermolecular distance between DOX molecules, potentially modulating the electron density and partial charge distribution, thereby enhancing the polarizability essential for the SERS effect.[72]

Subsequent SERS measurements were performed with DOX dissolved in 10% FBS. Figure 5b shows the SERS spectra of 3rd@$Al_2O_3$ substrates incubated with DOX in the 1−100 nM concentration range. A calibration curve, plotting the SERS signal located at 470 $cm^{-1}$ against DOX molar concentration, exhibited a linear response (in logarithmic scale, $R^2 > 0.98$, Figure 5d) estimating a highly promising experimental LOD of 1 nM. Indeed, no signal was detected at concentrations below 1 nM. The decrease in sensitivity from 100 pM for DOX detection in water to 1 nM for DOX detection in FBS can be ascribed to the heightened chemical complexity of FBS, which slightly influences DOX detection. Nevertheless, it is worth emphasizing that the signal at 470 $cm^{-1}$ remained fully resolved and visible, even in the presence of FBS, enabling accurate quantification of DOX. Despite having comparable LODs to those of complex SERS platforms,[73,74] our device offers a significant advantage in simplicity and low fabrication cost. Table S3 compares the LOD of our proposed platform with the LOD values of various analytical methods and substrates.

Consequently, NIs-$Al_2O_3$ substrates emerge as compelling candidates for SERS ultrasensitive detection systems for TDM applications. In this context, they prove valuable for monitoring DOX at remarkably low concentrations in biological media, below the clinically relevant concentration range and, in this case, for the monitoring of DOX at very low concentrations in biological media, below the clinically relevant concentration range.[27]

## 4. CONCLUSIONS

In conclusion, this study presents a significant advancement in the field of biosensing technology, particularly for the detection of therapeutic drugs.

We propose a novel biosensing platform for personalized medicine, offering rapid, cost-effective, and highly sensitive detection of DOX levels in biological fluids. By combining LSPR and SERS techniques, the platform addresses the limitations of traditional TDM methods while offering scalability and suitability for real-time health monitoring. This advance aligns with the goals of personalized medicine, facilitating tailored treatments that optimize therapeutic efficacy and minimize adverse effects for individual patients.

LSPR measurements, based on one deposition/dewetting cycle, are performed with DOX dissolved in water, bovine serum, and human serum, achieving an experimental LOD of 1 nM in water and 16 nM in both types of serum. Notably, the device accurately detected DOX in both diluted and undiluted blood serum of cancer patients, aligning with the literature-reported DOX concentration values for patients receiving similar drug doses.

Moreover, by tailoring the nanoislands with $Al_2O_3$ coverage in three cycles of gold deposition/dewetting, SERS measurements demonstrated higher sensitivity, with LODs of 100 pM and 1 nM in water and fetal bovine serum, respectively. Surface functionalization with organic linkers is unnecessary, and the detectability is achieved without the need for covalent binding of the drug, which is simply adsorbed onto nanostructures embedded on glass.

The biosensor's reproducibility and stability under various environmental conditions further enhance its potential for point-of-care diagnostics. The possibility of monitoring and adjusting treatment regimens based on real-time data holds great promise for optimizing therapeutic outcomes and minimizing side effects, ultimately improving patient care.

## ■ ASSOCIATED CONTENT

### Supporting Information

The Supporting Information is available free of charge at https://pubs.acs.org/doi/10.1021/acsanm.4c01827.

Figure S1. SEM image of (a) cross section of NIs embedded into glass after three cycles; (b) glass substrate after gold NI etching. Figure S2. Absorbance spectrum of DOX compared to those of (a) Au NIs (light blue curve) and (b) Au/$Al_2O_3$ core/shell NIs (red curve). Figure S3. LSPR shift of 1st Au nanoisland covered with $SiO_2$ and $Al_2O_3$. Figure S4. Study of (a) long term-stability under ambient conditions (darkness, room temperature) for extended periods, (b) Study of stability in a humid environment. Figure S5. Extinction spectra of the NIs upon incubation with the different concentrations of DOX dissolved in (a) water and (b) 10% FBS. Figure S6. Simulation of binding site occupation of DOX in water onto Au NIs. Figure S7. Contact angle trend of 10% FBS aqueous solution on the Au NIs surface as a function of DOX. Figure S8. Graphic method to estimate the unknown DOX concentration in blood serum of cancer patients who received DOX treatment. Figure S9. Example of reuse for four different samples. Figure S10. Formation of an organic layer of DOX molecules over the gold NI (1st) after one hour of incubation (100 nM). Figure S11. (a) Raman spectrum of DOX aqueous solution on control sample (glass@$Al_2O_3$); (b) SERS spectra performed for 10 nM DOX aqueous solution onto all sample; different DOX aqueous solutions analyzed onto (c) Au NIs (3rd) and (d) 1st @$Al_2O_3$. Summary of manufacturing cost and production yield of sensors—Table S1; estimation of the FBS, HS, and water on the Au NIs without DOX—Table S2; estimation of the DOX binding sites on the NIs; comparison of LOD values of different analytical methods and substrates—Table S3 (PDF)

## ■ AUTHOR INFORMATION

### Corresponding Authors

**Simona Bettini** − *Department of Biological and Environmental Sciences and Technologies, University of Salento, 73100 Lecce, Italy;* orcid.org/0000-0002-5506-5413; Email: simona.bettini@unisalento.it



https://doi.org/10.1021/acsanm.4c01827
ACS Appl. Nano Mater. 2024, 7, 18724−18736

**Daniela Simeone** − *Institute of Nanotechnology-CNR, 73100 Lecce, Italy;* orcid.org/0000-0002-4136-4965; Email: daniela.simeone@nanotec.cnr.it

### Authors

**Alessandra Quarta** − *Institute of Nanotechnology-CNR, 73100 Lecce, Italy;* orcid.org/0000-0003-1911-9864

**Massimo Cuscunà** − *Institute of Nanotechnology-CNR, 73100 Lecce, Italy;* orcid.org/0000-0002-4934-3376

**Daniela Lorenzo** − *Institute of Nanotechnology-CNR, 73100 Lecce, Italy*

**Gianmichele Epifani** − *Institute of Nanotechnology-CNR, 73100 Lecce, Italy*

**Giuseppe Gigli** − *Institute of Nanotechnology-CNR, 73100 Lecce, Italy; Department of Mathematics and Physics "Ennio De Giorgi", University of Salento, 73100 Lecce, Italy*

**Ludovico Valli** − *Department of Biological and Environmental Sciences and Technologies, University of Salento, 73100 Lecce, Italy;* orcid.org/0000-0002-6943-8647

**Jamil A. Aliyev** − *National Center of Oncology, Azerbaijan Republic Ministry of Health, Baku AZ1012, Azerbaijan*

**Elkhan E. Kazimov** − *National Center of Oncology, Azerbaijan Republic Ministry of Health, Baku AZ1012, Azerbaijan*

**Matanat J. Bakhishova** − *Institute of Biophysics, Ministry of Science and Education of the Republic of Azerbaijan, Baku AZ1171, Azerbaijan*

**Oktay K. Gasymov** − *Institute of Biophysics, Ministry of Science and Education of the Republic of Azerbaijan, Baku AZ1171, Azerbaijan;* orcid.org/0000-0001-7916-0354

Complete contact information is available at: https://pubs.acs.org/10.1021/acsanm.4c01827

### Notes

The authors declare no competing financial interest.

The research, concerning Preliminary clinical test of doxorubicin pharmacokinetics based on Plasmon sensor system, was performed in accordance with the tenets of the Declaration of Helsinki. Informed consent was obtained from donors of human blood after explanation of the nature and possible consequences of the study; and the procedures were approved by the Ethic review board of National Center of Oncology, Azerbaijan Republic Ministry of Health. Intravenous injections of the DOX and blood withdrawal from patients were performed by experienced nurse under supervision of the therapeutic oncologist.

## ■ ACKNOWLEDGMENTS

A.Q., M.C., and D.S. acknowledge the Italian Ministry of Research (MUR) under the complementary actions to the NRRP (PNC0000007) "Fit4MedRob—Fit for Medical Robotics" Grant (PNC0000007, CUP B53C22006960001) funded by NextGenerationEU. The authors also acknowledge the "Tecnopolo per la medicina di precisione" (TecnoMed Puglia)—Regione Puglia: DGR n.2117 del 21/11/2018, CUP: B84I18000540002 and "Tecnopolo di Nanotecnologia e Fotonica per la medicina di precisione" (TECNOMED)—FISR/MIUR-CNR: delibera CIPE n.3449 del 7-08-2017, CUP: B83B17000010001. The work was supported by the NRRP National projects "Nano Foundries and Fine Analysis—Digital Infrastructure" (NFFA-DI)—Code: IR0000015, CUP: B53C22004310006 financed by the NextGenerationEU. We acknowledge financial support under the National Recovery and Resilience Plan (NRRP), Mission 4, Component 2, Investment 1.1, Call for tender No. 104 published on 2.2.2022 by the Italian Ministry of University and Research (MUR), funded by the European Union—NextGenerationEU—Project Title: Biophotonic platforms and MUltivalent Surface Interactions for neXt-generation virus detection (MuSIx)—CUP B53D23004170006—Grant Assignment Decree No. 718 adopted on 25 May 2023 by the Italian Ministry of University and Research (MUR), and "I-PHOQS" Grant (CUP B53C22001750006) financed by the NextGenerationEU. D.S. is grateful to Dr. Adriano Cola for scientific discussions. The authors warmly acknowledge Prof. Robert C. Pullar from Ca' Foscari University of Venice for English review and editing.

## ■ REFERENCES

(1) Knezevic, C. E.; Clarke, W. Cancer Chemotherapy: The Case for Therapeutic Drug Monitoring. *Ther. Drug Monit.* **2020**, *42* (1), 6−19.

(2) Briki, M.; André, P.; Thoma, Y.; Widmer, N.; Wagner, A. D.; Decosterd, L. A.; Buclin, T.; Guidi, M.; Carrara, S. Precision Oncology by Point-of-Care Therapeutic Drug Monitoring and Dosage Adjustment of Conventional Cytotoxic Chemotherapies: A Perspective. *Pharmaceutics* **2023**, *15* (4), 1283.

(3) Ghirmai, S.; Mume, E.; Tolmachev, V.; Sjöberg, S. Synthesis and Radioiodination of Some Daunorubicin and Doxorubicin Derivatives. *Carbohydr. Res.* **2005**, *340* (1), 15−24.

(4) Krasnovskaya, O. O.; Malinnikov, V. M.; Dashkova, N. S.; Gerasimov, V. M.; Grishina, I. V.; Kireev, I. I.; Lavrushkina, S. V.; Panchenko, P. A.; Zakharko, M. A.; Ignatov, P. A.; Fedorova, O. A.; Jonusauskas, G.; Skvortsov, D. A.; Kovalev, S. S.; Beloglazkina, E. K.; Zyk, N. V.; Majouga, A. G. Thiourea Modified Doxorubicin: A Perspective pH-Sensitive Prodrug. *Bioconjugate Chem.* **2019**, *30* (3), 741−750.

(5) Zhang, S.; Liu, X.; Bawa-Khalfe, T.; Lu, L.-S.; Lyu, Y. L.; Liu, L. F.; Yeh, E. T. H. Identification of the Molecular Basis of Doxorubicin-Induced Cardiotoxicity. *Nat. Med.* **2012**, *18* (11), 1639−1642.

(6) Gerweck, L. E.; Kozin, S. V.; Stocks, S. J. The pH Partition Theory Predicts the Accumulation and Toxicity of Doxorubicin in Normal and Low-pH-Adapted Cells. *Br. J. Cancer* **1999**, *79* (5−6), 838−842.

(7) Kciuk, M.; Gielecińska, A.; Mujwar, S.; Kołat, D.; Kałuzińska-Kołat, Ż.; Celik, I.; Kontek, R. Doxorubicin—An Agent with Multiple Mechanisms of Anticancer Activity. *Cells* **2023**, *12* (4), 659.

(8) El-Kimary, E. I.; El-Yazbi, A. F. An Eco-Friendly Stability-Indicating Spectrofluorimetric Method for the Determination of Two Anticancer Stereoisomer Drugs in Their Pharmaceutical Preparations Following Micellar Enhancement: Application to Kinetic Degradation Studies. *Spectrochim. Acta, Part A* **2016**, *163*, 145−153.

(9) Daeihamed, M.; Haeri, A.; Dadashzadeh, S. A Simple and Sensitive HPLC Method for Fluorescence Quantitation of Doxorubicin in Micro-Volume Plasma: Applications to Pharmacokinetic Studies in Rats. *Iran J. Pharm. Res.* **2015**, *14* (Suppl), 33−42.

(10) Ibsen, S.; Su, Y.; Norton, J.; Zahavy, E.; Hayashi, T.; Adams, S.; Wrasidlo, W.; Esener, S. Extraction Protocol and Mass Spectrometry Method for Quantification of Doxorubicin Released Locally from Prodrugs in Tumor Tissue: Quantification of Local Tissue Prodrug Activation. *J. Mass Spectrom.* **2013**, *48* (7), 768−773.

(11) Zhang, K.; Zhang, Y. Electrochemical Behavior of Adriamycin at an Electrode Modified with Silver Nanoparticles and Multi-Walled Carbon Nanotubes, and Its Application. *Microchim. Acta* **2010**, *169* (1−2), 161−165.

(12) Soleymani, J.; Hasanzadeh, M.; Eskandani, M.; Khoubnasabjafari, M.; Shadjou, N.; Jouyban, A. Electrochemical Sensing of Doxorubicin in Unprocessed Whole Blood, Cell Lysate, and Human Plasma Samples Using Thin Film of Poly-Arginine Modified Glassy Carbon Electrode. *Mater. Sci. Eng., C* **2017**, *77*, 790−802.

(13) Sharifi, J.; Fayazfar, H. Highly Sensitive Determination of Doxorubicin Hydrochloride Antitumor Agent via a Carbon Nanotube/Gold Nanoparticle Based Nanocomposite Biosensor. *Bioelectrochemistry* **2021**, *139*, No. 107741.
(14) Materon, E. M.; Wong, A.; Fatibello-Filho, O.; Faria, R. C. Development of a Simple Electrochemical Sensor for the Simultaneous Detection of Anticancer Drugs. *J. Electroanal. Chem.* **2018**, *827*, 64−72.
(15) Damborský, P.; Švitel, J.; Katrlík, J. Optical Biosensors. *Essays Biochem.* **2016**, *60* (1), 91−100.
(16) Nieciecka, D.; Krysinski, P. Interactions of Doxorubicin with Self-Assembled Monolayer-Modified Electrodes: Electrochemical, Surface Plasmon Resonance (SPR), and Gravimetric Studies. *Langmuir* **2011**, *27* (3), 1100−1107.
(17) Zhao, J.; Zhang, X.; Yonzon, C. R.; Haes, A. J.; Van Duyne, R. P. Localized Surface Plasmon Resonance Biosensors. *Nanomedicine* **2006**, *1* (2), 219−228.
(18) Zhao, S. S.; Bichelberger, M. A.; Colin, D. Y.; Robitaille, R.; Pelletier, J. N.; Masson, J.-F. Monitoring Methotrexate in Clinical Samples from Cancer Patients during Chemotherapy with a LSPR-Based Competitive Sensor. *Analyst* **2012**, *137* (20), 4742.
(19) Naresh, V.; Lee, N. A Review on Biosensors and Recent Development of Nanostructured Materials-Enabled Biosensors. *Sensors* **2021**, *21* (4), 1109.
(20) Wang, P.; Lin, Z.; Su, X.; Tang, Z. Application of Au Based Nanomaterials in Analytical Science. *Nano Today* **2017**, *12*, 64−97.
(21) Bonyár, A.; Csarnovics, I.; Veres, M.; Himics, L.; Csik, A.; Kámán, J.; Balázs, L.; Kökényesi, S. Investigation of the Performance of Thermally Generated Gold Nanoislands for LSPR and SERS Applications. *Sens. Actuators, B* **2018**, *255*, 433−439.
(22) Xiao, T.; Huang, J.; Wang, D.; Meng, T.; Yang, X. Au and Au-Based Nanomaterials: Synthesis and Recent Progress in Electrochemical Sensor Applications. *Talanta* **2020**, *206*, No. 120210.
(23) Jin, C.; Wu, Z.; Molinski, J. H.; Zhou, J.; Ren, Y.; Zhang, J. X. J. Plasmonic Nanosensors for Point-of-Care Biomarker Detection. *Mater. Today Bio* **2022**, *14*, No. 100263.
(24) Zhou, J.; Tao, F.; Zhu, J.; Lin, S.; Wang, Z.; Wang, X.; Ou, J.-Y.; Li, Y.; Liu, Q. H. Portable Tumor Biosensing of Serum by Plasmonic Biochips in Combination with Nanoimprint and Microfluidics. *Nanophotonics* **2019**, *8* (2), 307−316.
(25) Langer, J.; Jimenez de Aberasturi, D.; Aizpurua, J.; Alvarez-Puebla, R. A.; Auguié, B.; Baumberg, J. J.; Bazan, G. C.; Bell, S. E. J.; Boisen, A.; Brolo, A. G.; Choo, J.; Cialla-May, D.; Deckert, V.; Fabris, L.; Faulds, K.; García de Abajo, F. J.; Goodacre, R.; Graham, D.; Haes, A. J.; Haynes, C. L.; Huck, C.; Itoh, T.; Käll, M.; Kneipp, J.; Kotov, N. A.; Kuang, H.; Le Ru, E. C.; Lee, H. K.; Li, J.-F.; Ling, X. Y.; Maier, S. A.; Mayerhöfer, T.; Moskovits, M.; Murakoshi, K.; Nam, J.-M.; Nie, S.; Ozaki, Y.; Pastoriza-Santos, I.; Perez-Juste, J.; Popp, J.; Pucci, A.; Reich, S.; Ren, B.; Schatz, G. C.; Shegai, T.; Schlücker, S.; Tay, L.-L.; Thomas, K. G.; Tian, Z.-Q.; Van Duyne, R. P.; Vo-Dinh, T.; Wang, Y.; Willets, K. A.; Xu, C.; Xu, H.; Xu, Y.; Yamamoto, Y. S.; Zhao, B.; Liz-Marzán, L. M. Present and Future of Surface-Enhanced Raman Scattering. *ACS Nano* **2020**, *14* (1), 28−117.
(26) Han, X. X.; Rodriguez, R. S.; Haynes, C. L.; Ozaki, Y.; Zhao, B. Surface-Enhanced Raman Spectroscopy. *Nat. Rev. Methods Primers* **2021**, *1* (1), No. 87.
(27) Sun, F.; Hung, H.-C.; Sinclair, A.; Zhang, P.; Bai, T.; Galvan, D. D.; Jain, P.; Li, B.; Jiang, S.; Yu, Q. Hierarchical Zwitterionic Modification of a SERS Substrate Enables Real-Time Drug Monitoring in Blood Plasma. *Nat. Commun.* **2016**, *7* (1), No. 13437.
(28) Panikar, S. S.; Banu, N.; Escobar, E.-R.; García, G.-R.; Cervantes-Martínez, J.; Villegas, T.-C.; Salas, P.; De la Rosa, E. Stealth Modified Bottom up SERS Substrates for Label-Free Therapeutic Drug Monitoring of Doxorubicin in Blood Serum. *Talanta* **2020**, *218*, No. 121138.
(29) Wang, Y.; Yu, C.; Ji, H.; Liu, Z.; Wang, X.; Ji, Y.; Sun, X.; Zhao, Y.; Qiu, X.; Zhang, T.; Li, J.; Liu, X.; Lv, X.; Cai, B.; Zhao, Y.; Huang, J.-A.; Li, Y. Label-Free Therapeutic Drug Monitoring in Human Serum by the 3-Step Surface Enhanced Raman Spectroscopy and Multivariate Analysis. *Chem. Eng. J.* **2023**, *452*, No. 139588.
(30) Hu, Y.; Hu, Y.; Wang, Z.; Yong, J.; Xiong, W.; Wu, D.; Xu, S. Efficient Concentration of Trace Analyte with Ordered Hotspot Construction for a Robust and Sensitive SERS Platform. *Int. J. Extreme Manuf.* **2024**, *6* (3), No. 035505.
(31) Lin, C.; Li, Y.; Peng, Y.; Zhao, S.; Xu, M.; Zhang, L.; Huang, Z.; Shi, J.; Yang, Y. Recent Development of Surface-Enhanced Raman Scattering for Biosensing. *J. Nanobiotechnol.* **2023**, *21* (1), No. 149.
(32) Yeh, Y.-J.; Cho, C.-J.; Benas, J.-S.; Tung, K.-L.; Kuo, C.-C.; Chiang, W.-H. Plasma-Engineered Plasmonic Nanoparticle-Based Stretchable Nanocomposites as Sensitive Wearable SERS Sensors. *ACS Appl. Nano Mater.* **2023**, *6* (12), 10115−10125.
(33) Yeh, Y.-J.; Le, T.-N.; Hsiao, W. W.-W.; Tung, K.-L.; Ostrikov, K. Ken.; Chiang, W.-H. Plasmonic Nanostructure-Enhanced Raman Scattering for Detection of SARS-CoV-2 Nucleocapsid Protein and Spike Protein Variants. *Anal. Chim. Acta* **2023**, *1239*, No. 340651.
(34) Vaiani, L.; Boccaccio, A.; Uva, A. E.; Palumbo, G.; Piccininni, A.; Guglielmi, P.; Cantore, S.; Santacroce, L.; Charitos, I. A.; Ballini, A. Ceramic Materials for Biomedical Applications: An Overview on Properties and Fabrication Processes. *J. Funct. Biomater.* **2023**, *14* (3), 146.
(35) Yang, Y.; Peng, Y.; Lin, C.; Long, L.; Hu, J.; He, J.; Zeng, H.; Huang, Z.; Li, Z.-Y.; Tanemura, M.; Shi, J.; Lombardi, J. R.; Luo, X. Human ACE2-Functionalized Gold "Virus-Trap" Nanostructures for Accurate Capture of SARS-CoV-2 and Single-Virus SERS Detection. *Nano-Micro Lett.* **2021**, *13* (1), No. 109.
(36) Xiao, Y.; Zhang, Z.; Yin, S.; Ma, X. Nanoplasmonic Biosensors for Precision Medicine. *Front. Chem.* **2023**, *11*, No. 1209744.
(37) Aspnes, D. E.; Studna, A. A. Dielectric Functions and Optical Parameters of Si, Ge, GaP, GaAs, GaSb, InP, InAs, and InSb from 1.5 to 6.0 eV. *Phys. Rev. B* **1983**, *27* (2), 985−1009.
(38) Herzinger, C. M.; Johs, B.; McGahan, W. A.; Woollam, J. A.; Paulson, W. Ellipsometric Determination of Optical Constants for Silicon and Thermally Grown Silicon Dioxide via a Multi-Sample, Multi-Wavelength, Multi-Angle Investigation. *J. Appl. Phys.* **1998**, *83* (6), 3323−3336.
(39) Langereis, E.; Heil, S. B. S.; Knoops, H. C. M.; Keuning, W.; Van De Sanden, M. C. M.; Kessels, W. M. M. *In Situ* Spectroscopic Ellipsometry as a Versatile Tool for Studying Atomic Layer Deposition. *J. Phys. D: Appl. Phys.* **2009**, *42* (7), No. 073001.
(40) Karakouz, T.; Tesler, A. B.; Sannomiya, T.; Feldman, Y.; Vaskevich, A.; Rubinstein, I. Mechanism of Morphology Transformation during Annealing of Nanostructured Gold Films on Glass. *Phys. Chem. Chem. Phys.* **2013**, *15* (13), 4656.
(41) Karakouz, T.; Tesler, A. B.; Bendikov, T. A.; Vaskevich, A.; Rubinstein, I. Highly Stable Localized Plasmon Transducers Obtained by Thermal Embedding of Gold Island Films on Glass. *Adv. Mater.* **2008**, *20* (20), 3893−3899.
(42) Tesler, A. B.; Maoz, B. M.; Feldman, Y.; Vaskevich, A.; Rubinstein, I. Solid-State Thermal Dewetting of Just-Percolated Gold Films Evaporated on Glass: Development of the Morphology and Optical Properties. *J. Phys. Chem. C* **2013**, *117* (21), 11337−11346.
(43) Wagner, R. S.; Ellis, W. C. VAPOR-LIQUID-SOLID MECHANISM OF SINGLE CRYSTAL GROWTH. *Appl. Phys. Lett.* **1964**, *4* (5), 89−90.
(44) Cuscunà, M.; Convertino, A.; Mariucci, L.; Fortunato, G.; Felisari, L.; Nicotra, G.; Spinella, C.; Pecora, A.; Martelli, F. Low-Temperature, Self-Catalyzed Growth of Si Nanowires. *Nanotechnology* **2010**, *21* (25), No. 255601.
(45) Ray, N. J.; Yoo, J. H.; McKeown, J. T.; Elhadj, S.; Baxamusa, S. H.; Johnson, M. A.; Nguyen, H. T.; Steele, W. A.; Chesser, J. M.; Matthews, M. J.; Feigenbaum, E. Enhanced Tunability of Gold Nanoparticle Size, Spacing, and Shape for Large-Scale Plasmonic Arrays. *ACS Appl. Nano Mater.* **2019**, *2* (7), 4395−4401.
(46) Ray, N. J.; Yoo, J.-H.; Baxamusa, S.; Nguyen, H. T.; Elhadj, S.; Feigenbaum, E. Tuning Gold Nanoparticle Size with Fixed Interparticle Spacing in Large-Scale Arrays: Implications for


https://doi.org/10.1021/acsanm.4c01827
*ACS Appl. Nano Mater.* 2024, 7, 18724−18736

Plasmonics and Nanoparticle Etching Masks. *ACS Appl. Nano Mater.* **2021**, *4* (3), 2733−2742.
(47) Lorenzo, D.; Riminucci, F.; Manoccio, M.; Balestra, G.; Simeone, D.; Tobaldi, D. M.; Esposito, M.; Passaseo, A.; Tasco, V.; Cuscunà, M. Molybdenum Oxide Functional Passivation of Aluminum Dimers for Enhancing Optical-Field and Environmental Stability. *Photonics* **2022**, *9* (8), 523.
(48) Deng, L.; Zhai, Y.; Chen, Y.; Wang, N.; Huang, Y. Enhancing the Plasmonic Fields by a High Refractive Index Dielectric Coating for Surface Enhanced Spectroscopies. *J. Phys. D: Appl. Phys.* **2019**, *52* (43), No. 43LT01.
(49) Kang, M.; Park, S.-G.; Jeong, K.-H. Repeated Solid-State Dewetting of Thin Gold Films for Nanogap-Rich Plasmonic Nanoislands. *Sci. Rep.* **2015**, *5* (1), No. 14790.
(50) Deng, L.; Zhai, Y.; Chen, Y.; Wang, N.; Huang, Y. Enhancing Local Electric Fields at Plasmonic Nanogaps by Optimal Dielectric Coatings. *J. Phys. D: Appl. Phys.* **2020**, *53* (15), No. 155103.
(51) Simeone, D.; Tasco, V.; Esposito, M.; Manoccio, M.; Lorenzo, D.; Scuderi, M.; Luca, A. D.; Cabrini, S.; Passaseo, A.; Cuscunà, M. Near-Field Enhancement in Oxidized Close Gap Aluminum Dimers. *Nanotechnology* **2021**, *32* (2), No. 025305.
(52) Rajesh, C.; Nigam, S.; Majumder, C. The Structural and Electronic Properties of $Au_n$ Clusters on the $\alpha$-$Al_2O_3$ (0001) Surface: A First Principles Study. *Phys. Chem. Chem. Phys.* **2014**, *16* (48), 26561−26569.
(53) Candreva, A.; Lewandowski, W.; La Deda, M. Thickness Control of the Silica Shell: A Way to Tune the Plasmonic Properties of Isolated and Assembled Gold Nanorods. *J. Nanopart. Res.* **2022**, *24* (2), No. 19.
(54) Simeone, D.; Esposito, M.; Scuderi, M.; Calafiore, G.; Palermo, G.; De Luca, A.; Todisco, F.; Sanvitto, D.; Nicotra, G.; Cabrini, S.; Tasco, V.; Passaseo, A.; Cuscunà, M. Tailoring Electromagnetic Hot Spots toward Visible Frequencies in Ultra-Narrow Gap $Al/Al_2O_3$ Bowtie Nanoantennas. *ACS Photonics* **2018**, *5* (8), 3399−3407.
(55) Komaee, K.; Friedman, G.; Dan, N. The Kinetics and Saturation of Reversible Adsorption on Patterned (Heterogeneous) Surfaces. *Langmuir* **2006**, *22* (3), 871−876.
(56) Yockell-Lelièvre, H.; Bukar, N.; McKeating, K. S.; Arnaud, M.; Cosin, P.; Guo, Y.; Dupret-Carruel, J.; Mougin, B.; Masson, J.-F. Plasmonic Sensors for the Competitive Detection of Testosterone. *Analyst* **2015**, *140* (15), 5105−5111.
(57) Agudelo, D.; Bourassa, P.; Bruneau, J.; Bérubé, G.; Asselin, É.; Tajmir-Riahi, H.-A. Probing the Binding Sites of Antibiotic Drugs Doxorubicin and N-(Trifluoroacetyl) Doxorubicin with Human and Bovine Serum Albumins. *PLoS One* **2012**, *7* (8), No. e43814.
(58) Moirangthem, R. S.; Yaseen, M. T.; Wei, P.-K.; Cheng, J.-Y.; Chang, Y.-C. Enhanced Localized Plasmonic Detections Using Partially-Embedded Gold Nanoparticles and Ellipsometric Measurements. *Biomed. Opt. Express* **2012**, *3* (5), 899.
(59) Yaseen, M. T.; Chen, M.; Chang, Y.-C. Partially Embedded Gold Nanoislands in a Glass Substrate for SERS Applications. *RSC Adv.* **2014**, *4* (98), 55247−55251.
(60) Harahap, Y.; Ardiningsih, P.; Corintias Winarti, A.; Purwanto, D. J. Analysis of the Doxorubicin and Doxorubicinol in the Plasma of Breast Cancer Patients for Monitoring the Toxicity of Doxorubicin. *Drug Des., Dev. Ther.* **2020**, *14*, 3469−3475.
(61) Barpe, D. R.; Rosa, D. D.; Froehlich, P. E. Pharmacokinetic Evaluation of Doxorubicin Plasma Levels in Normal and Overweight Patients with Breast Cancer and Simulation of Dose Adjustment by Different Indexes of Body Mass. *Eur. J. Pharm. Sci.* **2010**, *41* (3−4), 458−463.
(62) Luu, A. Z.; Chowdhury, B.; Al-Omran, M.; Teoh, H.; Hess, D. A.; Verma, S. Role of Endothelium in Doxorubicin-Induced Cardiomyopathy. *J. Am. Coll. Cardiol. Basic Transl. Sci.* **2018**, *3* (6), 861−870.
(63) Beljebbar, A.; Sockalingum, G. D.; Angiboust, J. F.; Manfait, M. Comparative FT SERS, Resonance Raman and SERRS Studies of Doxorubicin and Its Complex with DNA. *Spectrochim. Acta, Part A* **1995**, *51* (12), 2083−2090.
(64) Smulevich, G.; Feis, A. Surface-Enhanced Resonance Raman Spectra of Adriamycin, 11-Deoxycarminomycin, Their Model Chromophores, and Their Complexes with DNA. *J. Phys. Chem. A* **1986**, *90* (23), 6388−6392.
(65) Nabiev, I. R.; Morjani, H.; Manfait, M. Selective Analysis of Antitumor Drug Interaction with Living Cancer Cells as Probed by Surface-Enhanced Raman Spectroscopy. *Eur. Biophys. J.* **1991**, *19* (6), 311−316.
(66) Farhane, Z.; Bonnier, F.; Casey, A.; Byrne, H. J. Raman Micro Spectroscopy for in Vitro Drug Screening: Subcellular Localisation and Interactions of Doxorubicin. *Analyst* **2015**, *140* (12), 4212−4223.
(67) Yan, Q.; Priebe, W.; Chaires, J. B.; Czernuszewicz, R. S. Interaction of Doxorubicin and Its Derivatives with DNA: Elucidation by Resonance Raman and Surface-Enhanced Resonance Raman Spectroscopy. *Biospectroscopy* **1997**, *3* (4), 307−316.
(68) Gautier, J.; Munnier, E.; Douziech-Eyrolles, L.; Paillard, A.; Dubois, P.; Chourpa, I. SERS Spectroscopic Approach to Study Doxorubicin Complexes with Fe2+ Ions and Drug Release from SPION-Based Nanocarriers. *Analyst* **2013**, *138* (24), 7354.
(69) Baffou, G.; Cichos, F.; Quidant, R. Applications and Challenges of Thermoplasmonics. *Nat. Mater.* **2020**, *19* (9), 946−958.
(70) Wang, L.; Feng, Y.; Li, Z.; Liu, G. Nanoscale Thermoplasmonic Welding. *iScience* **2022**, *25* (6), No. 104422.
(71) Bettini, S.; Pagano, R.; Semeraro, P.; Ottolini, M.; Salvatore, L.; Marzo, F.; Lovergine, N.; Giancane, G.; Valli, L. $SiO_2$-Coated ZnO Nanoflakes Decorated with Ag Nanoparticles for Photocatalytic Water Oxidation. *Chem. - Eur. J.* **2019**, *25* (62), 14123−14132.
(72) Poudel, L.; Wen, A. M.; French, R. H.; Parsegian, V. A.; Podgornik, R.; Steinmetz, N. F.; Ching, W.-Y. Electronic Structure and Partial Charge Distribution of Doxorubicin in Different Molecular Environments. *ChemPhysChem* **2015**, *16* (7), 1451−1460.
(73) Kaja, S.; Mathews, A. V.; Venuganti, V. V. K.; Nag, A. Bimetallic Ag−Cu Alloy SERS Substrates as Label-Free Biomedical Sensors: Femtomolar Detection of Anticancer Drug Mitoxantrone with Multiplexing. *Langmuir* **2023**, *39* (15), 5591−5601.
(74) Eskandari, V.; Sahbafar, H.; Zeinalizad, L.; Mahmoudi, R.; Karimpour, F.; Hadi, A.; Bardania, H. Coating of Silver Nanoparticles (AgNPs) on Glass Fibers by a Chemical Method as Plasmonic Surface-Enhanced Raman Spectroscopy (SERS) Sensors to Detect Molecular Vibrations of Doxorubicin (DOX) Drug in Blood Plasma. *Arabian J. Chem.* **2022**, *15* (8), No. 104005.


https://doi.org/10.1021/acsanm.4c01827
*ACS Appl. Nano Mater.* 2024, 7, 18724−18736